Investigating the accuracy of continuum models for the simulation of industrial maleic anhydride reactors: A comparative single particle CFD study

Scott D. Anderson [a,*], Martin Kutscherauer [a,b], Sebastian Böcklein [b], Gerhard Mestl [b], Thomas Turek [a], Gregor D. Wehinger [a]

[a] *Institute of Chemical and Electrochemical Process Engineering, Clausthal University of Technology, Leibnizstraße 17, Clausthal-Zellerfeld, 38678, Germany*
[b] *Clariant AG, Waldheimer Strasse 15, Heufeld, 83052, Germany*

ARTICLE INFO

ABSTRACT

The selective oxidation of *n*-butane to maleic anhydride is a strongly exothermic reaction. Resulting local hot-spots and intraparticle temperatures high above the surrounding fluid temperature are challenging for safe and economic operation of reactors. Detailed modelling on all length scales is therefore required for an accurate description of this process. In this contribution, the one dimensional description of the ring-shaped catalyst, commonly used in continuum reactor modelling, is compared to three dimensional computational fluid dynamics simulations for the case of a single catalyst particle at different inclination angles (0 to 90°). Polytropic chemical reaction is considered under typical *n*-butane oxidation conditions ($Re_p = 400$), representing a catalyst particle close to the inlet, ($T = 673$ K) and at the hot-spot ($T = 730$ K) of an industrial reactor. Comparative analysis suggests that the one dimensional simplification is justified when external transport phenomena are not the limiting resistance. Otherwise, neglecting two spatial dimensions leads to erroneous predictions.

1. Introduction

Maleic anhydride (MA) is an organic molecule that plays an important role in the chemical industries as monomer and also as a precursor to lubricants and pesticides. State of the art processes use vanadium phosphorous oxide (VPO) catalysts to selectively oxidise *n* butane to MA. Because of the strongly exothermic nature of the reaction ($\Delta_R H^0 = -1{,}236 \, \text{kJ} \, \text{mol}^{-1}$), it is usually carried out in, multitubular fixed bed reactors with small tube diameters, where the heat of reaction is removed via a shell side salt bath at temperatures between 390 and 430 °C. Although *n* butane feed concentrations are rather low (< 1.8 vol %), distinct hot spots of up to 70 K in the reactor and temperature differences of up to 40 K on the catalyst particle can occur, nonetheless (Mestl et al., 2016; Dong et al., 2018; Müller et al., 2020, 2021, 2022). Further enhancing the importance of thermal control is the loss of phosphorous from the VPO catalyst, occurring at high temperatures. This leads to increased catalytic activity that favours the total oxidation of *n* butane, which releases even more heat than the selective oxidation, but more importantly reduces the selectivity toward the target product MA in favour of the carbon oxides CO and CO_2. In addition to economic

considerations, selective oxidation reactions of any kind, including the synthesis of MA, face additional scrutiny by political pressure to reduce carbon emissions in view of climate change (National Research Council, 2001). Industrially, this effect is countered by adding trimethyl phosphate to the feed stream (Mestl et al., 2016; Müller et al., 2022). Safe and economic operation of reactors, as well as reactor design, requires accurate description of all processes taking place in the reactor. Accurate description in turn requires detailed modelling on all involved length scales: from reactor scale (e.g. salt bath temperature distribution, local hot spots) over particle scale (e.g. intraparticle temperature gradients) up to the molecular scale (e.g. reaction kinetics). Potential for improvement is given especially on the molecular and particle scale when it comes to the phosphorous dynamics of the VPO catalyst. Only few models exist to describe the sorption processes at the catalyst surface and distribution of the phosphorous species within the fixed bed (Mestl et al., 2016). The aforementioned challenges are not limited to the selective oxidation of *n* butane but rather apply to any selective oxidation process (Hermans et al., 2009).

To date, it is common practice to use continuum models to design industrial MA reactors (Müller et al., 2021). This modelling approach

---

* Corresponding author.

E-mail addresses: anderson@icvt.tu-clausthal.de (S.D. Anderson), kutscherauer@icvt.tu-clausthal.de (M. Kutscherauer), Sebastian.Boecklein@clariant.com (S. Böcklein), Gerhard.Mestl@clariant.com (G. Mestl), turek@icvt.tu-clausthal.de (T. Turek), wehinger@icvt.tu-clausthal.de (G.D. Wehinger).

consists of the description of the fixed bed geometry as a discretised domain, which can be one or two dimensional (1D, 2D), and over which the governing equations are solved. Continuum models can vary widely with respect to their sophistication. The solid phase can either be lumped together with the fluid phase (pseudo homogeneous) or be considered with separately discretised balance equations (heterogeneous). Thereby, a wide range of model formulations are conceivable ranging from the simple 1D pseudo homogeneous to the 2D 2D heterogeneous model. Of course, with increasing level of detail the complexity of the model and the computational cost increase as well (Müller et al., 2021; Wehinger et al., 2022; Froment et al., 1990). The literature concerning modelling of MA reactors features almost the entire spectrum of conceivable model arrangements. Two recent studies by Maußner and Freund (2018) and Petric and Karić (2019) used pseudo homogeneous 1D models to optimise the operation of an industrial MA reactor for an uncertain feedstock composition and to investigate the models ability to reproduce data from an industrial MA reactor using different kinetic models, respectively. Wellauer et al. (1986) formulated a 1D 1D heterogeneous model to derive best practices for MA reactor operation. The 1D 1D heterogeneous approach was also adopted by Sharma et al. (1991), who derived power law kinetics for the selective oxidation of n butane and by Diedenhoven et al. (2012), who studied a model for the phosphorous dynamics of the VPO catalyst. The recently published kinetic model by Müller et al. (2021) was also developed using a 1D 1D heterogeneous model of a micro fixed bed reactor, filled with milled catalyst. Brandstädter and Kraushaar Czarnetzki (2007) developed a 2D homogeneous reactor model to simulate an industrial scale MA reactor. Both Lesser et al. (2017) and Dong et al. (2016) used 2D 1D heterogeneous models in their studies. The latter discovered via simulations that higher MA yields could be achieved using a catalyst with bi modal pore size distribution.

Exact solutions of the reaction/diffusion equation to consider the shape of the particle in the reaction/diffusion equation only exist for spheres or infinitely long slabs and cylinders. Much work has been dedicated to derive models that approximate more elaborate particle shapes, such as rings, trilobes, multi hole cylinders or even the double α shape which find widespread use in the chemical industries (Afandizadeh and Foumeny, 2001; Karthik and Buwa, 2019; Reitzmann et al., 2016). The development of these models has been ongoing since the last century (Burghardt and Kubaczka, 1996). The Baretto group from the Universidad Nacional de La Plata, Argentina, published several works featuring different approaches to describing complex particle shapes for 1D models and tested these extensively against 3D simulations, both for theoretical kinetics and practical reaction systems (Mariani et al., 2003; Mocciaro et al., 2011; Mariani et al., 2013; Taulamet et al., 2018). In a recent publication, Donaubauer and Hinrichsen (2019) tested one of the models published by Mariani et al. (2003, 2013) for nine different catalyst shapes against three dimensional (3D) solutions and found excellent agreement for both intraparticle profiles and global effectiveness factors. Further, the external flow and transport phenomena in the stagnant film around particles are usually described via engineering correlations (Wehinger et al., 2022). In a study published by Dixon (2014), heat and mass transfer concerning a single catalyst particle were investigated via computational fluid dynamics (CFD) simulations covering the behaviour at different inclination angles relative to the flow for steam methane reforming under industrial conditions. Dixon found that an inclination angle around 45° were favourable for both heat and mass transfer. Besides the fact that only approximate solutions exist to describe commonly used particle shapes, it is well known that an individual particle in a catalytic fixed bed can experience a wide range of physical conditions (such as temperature or species concentrations) on its surface (Dong et al., 2018). Since individual particles are not considered in continuum models, this range of different physical conditions cannot be described either. As stated earlier, safe and economic reactor operation and design warrants exact knowledge about the relation between intraparticle transport phenomena and catalytic reaction. It is therefore a cardinal requirement to verify that continuum models, despite their simplifying assumptions, remain able to describe those.

In this study we aim to assess whether the neglect of spatial dimensions impacts the ability of the continuum models to describe accurately the behaviour of a catalyst particle under n butane oxidation conditions. For this undertaking, intraparticle data resolved in 3D is required as reference. Only few studies cover the topic of intraparticle measurements however, due to the invasive nature and great effort accompanied (Sosna et al., 2020). Instead, in this work we employ CFD simulations allow to comfortably access intraparticle data. Simulations are conducted for a single VPO catalyst particle in external flow, considering the chemical reactions involved in selective n butane oxidation using the reaction kinetic model of Müller et al. (2021). We conduct 3D CFD simulations as well as 1D continuum model simulations in order to assess the 1D models ability to accurately represent the 3D results. Per the aforementioned comparison we aim to verify whether continuum models are an appropriate tool to design MA reactors considering the thermal challenges associated with this reaction system.

2. Methods

Simulations were conducted for two different sets of conditions, corresponding to a representative particle close to the inlet and one in the hot spot region of an industrial MA reactor. These conditions were determined from a 1D 1D heterogeneous model of a full sized industrial MA reactor, and are given in Table 1.

The 3D nature of the CFD model allows us to investigate the influence of the inclination angle, where we considered four different angles from 0° to 90°, which are visualised in Fig. 1.

The commercial CFD code Simcenter STAR CCM+ 2022.01 (Siemens PLM, 2022) was used to create the 3D model and to conduct the CFD simulations. Two 1D model formulations are used, which differ in how the 3D shape is described in the 1D formulation. 1D models were created and solved in the commercial package gPROMS ModelBuilder 7.0.7. Fig. 2 outlines the basic features of both model formulations for the ring shaped catalyst considered in this work. In the following, the formulations for each model are briefly summarised.

2.1. 1D ∞ Ring model

The ∞ Ring model is based on the analytical solution for an infinite cylinder. By means of a coordinate transformation, the model is manipulated in a manner that it corresponds to an infinite ring. That is, fluxes are considered only in the radial direction reaching from an inner to an outer surface. As the ring is considered infinitely long, axial fluxes are entirely neglected, as shown by the solid line indicating a diffusion barrier in Fig. 2.

Eq. (1) shows the coordinate transformation, where r is the dimensional radial coordinate, R_{inner} and R_{outer} are the inner and outer radius, and $\tilde{r}$ is the dimensionless radial coordinate.

$$\tilde{r} = \frac{r - R_{\text{inner}}}{R_{\text{outer}} - R_{\text{inner}}} \tag{1}$$

A mass balance according to Eq. (2) is solved for $n-1$ species, whereas the molar fluxes for the nth species are calculated through a closure condition, which states that the sum of all mass fluxes must be zero (Eq. (3)). This condition is best applied to a species that partakes in the chemical reaction, but is present in excess, which in the case considered in this study was chosen to be O_2.

$$\frac{\partial N_i}{\partial r} + \frac{1}{r} N_i = \sum^{j} (v_{i,j}\, r_j) \tag{2}$$

$$M_i \cdot N_i = -\sum_{\substack{k=1 \\ k \neq i}}^{n} M_k \cdot N_k \tag{3}$$

Table 1
Physical values for the representative inlet and hot-spot conditions.

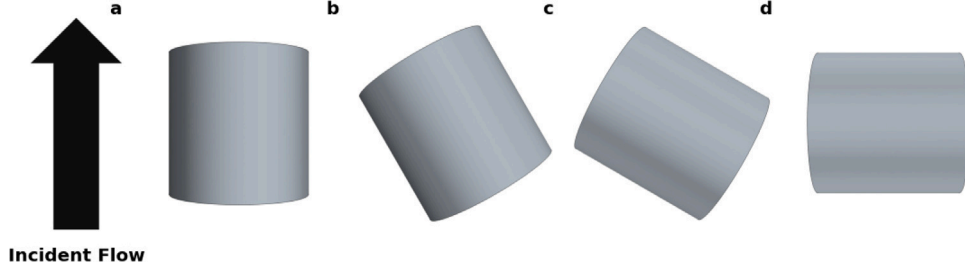|	T_{bulk} K	p Pa	Re_p –	w_{CO} –	w_{CO_2} –	$w_{C_4H_{10}}$ –	w_{H_2O} –	w_{MA} –	w_{O_2} –
Inlet	673	400	101325	0	0	0.030	0	0	0.226
Hot-spot	730	400	101325	0.002	0.003	0.026	0.011	0.010	0.203

Fig. 1. In the present study, a ring shaped catalytic particle is investigated at four different inclination angles between 0° and 90°.
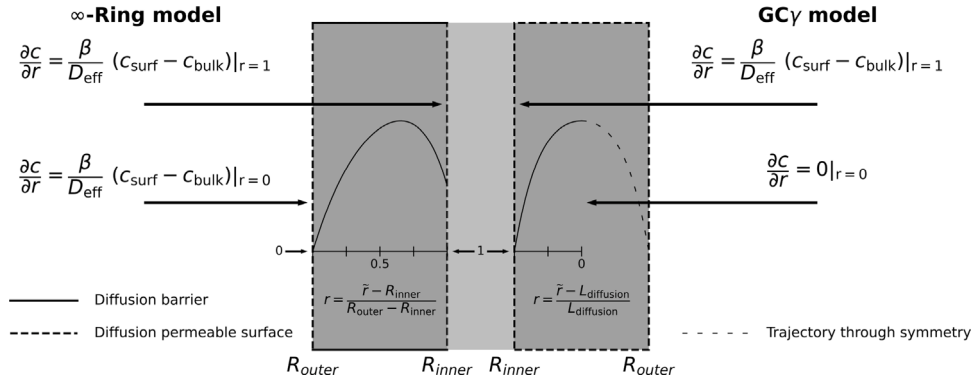

Fig. 2. The salient features of the ∞-Ring and the GCγ model, illustrated for a ring shaped catalyst particle.

Here, N_i are the molar fluxes for species i, $\nu_{i,j}$ is the stoichiometric coefficient of species i for reaction j and r_j is the rate for reaction j. As the model considers the inner and outer surface of the ring, a Robin boundary condition, outlined in Eq. (4) and visualised in Fig. 2, is applied at $\tilde{r} = 0$ and $\tilde{r} = 1$.

$$N_i = \beta_i(c_i - c_{i,bulk}) \tag{4}$$

β_i is the film mass transfer coefficient, and c_i is the species concentration. The molar fluxes are calculated using a Fickian formulation, given in Eq. (5), where for the solid particle an effective diffusion coefficient D_{eff}.

$$N_i = -D_{eff,i}\frac{\partial c_i}{\partial r} \tag{5}$$

The effective diffusion coefficient is calculated according to the Wilke Bosanquet equation (Bosanquet, 1944) (Eq. (6)) from the Knudsen diffusion coefficient D_k and the bulk fluid diffusion coefficient D_{mix}. Knudsen diffusion is calculated according to Eq. (7), where ϵ is the porosity, and ξ is the tortuosity (Aris, 1975). The bulk fluid diffusion coefficients are calculated from Eq. (8) according to the Wilke rule (Fairbanks and Wilke, 1950) using binary diffusion coefficients $D_{i,j}$, which are in turn derived using the empirical method by Fuller (Fuller et al., 1966, 1969) in Eq. (9). Here, x is the species mole fraction, $\Delta\upsilon$ is the diffusion volume of species i.

$$D_{eff,i} = \frac{\epsilon}{\xi}\left(\frac{1}{D_{k,i}} + \frac{1}{D_{mix,i}}\right)^{-1} \tag{6}$$

$$D_{k,i} = \frac{2}{3}r_{pore}\sqrt{\frac{8R_{gas}T}{\pi M}} \tag{7}$$

$$D_{mix,i} = \frac{1-x_i}{\sum_{\substack{j=1\\j\neq i}}^{n}\frac{x_j}{D_{i,j}}} \tag{8}$$

$$\left[\frac{D_{i,j}}{cm^2s^{-1}}\right] = \frac{0.00143\left[\frac{T}{K}\right]^{1.75}\sqrt{\left[\frac{M_i}{g\ mol^{-1}}\right]^{-1} + \left[\frac{M_j}{g\ mol^{-1}}\right]^{-1}}}{\frac{p}{bar}\sqrt{2}\left(\Delta\upsilon_i^{1/3} + \Delta\upsilon_j^{1/3}\right)^2} \tag{9}$$

The energy balance is given in Eq. (10) with λ being the effective thermal conductivity of the porous catalyst, T the temperature and $\Delta_r H_j$ is the heat of reaction.

$$\lambda\frac{\partial^2 T}{\partial r^2} + \lambda\frac{1}{r}\frac{\partial T}{\partial r} = \sum^{j} -\Delta_r H_j \cdot r_j \tag{10}$$

Again, the ∞ Ring model employs a Robin boundary conditions for both surfaces.

$$\lambda\frac{\partial T}{\partial r} = \begin{cases} \alpha(T - T_{bulk}) & \text{for } \tilde{r} = 0 \\ \alpha(T_{bulk} - T) & \text{for } \tilde{r} = 1 \end{cases} \tag{11}$$

2.2. 1D GCγ model

The generalised cylinder (GCγ) model was developed by Mariani et al. (2003) to describe any arbitrary particle shapes. It derives a representative cylinder with a custom diffusion length L_{diff} and a shape factor σ based on the original particle shape. The diffusion length spans from the surface of the representative cylinder to its centre. Since both model formulations are fairly similar, only the differences to the ∞ Ring model will be discussed here.

Based on a reaction/diffusion equation for a catalyst particle of homogeneous catalytic activity, the dimensionless Poisson problem,

given in Eq. (14), is derived. This then has to be solved for the desired particle shape, in order to derive a shape factor γ, from which a diffusion length for a representative cylinder is obtained. Boundary conditions are $G = 0$ at outside surfaces and $\nabla G = 0$ for symmetric surfaces, see Eqs. (12) and (13).

$$\nabla G = -1 \tag{12}$$

$$G = 0 \; \forall \; \text{outer surfaces} \tag{13}$$

$$\nabla G = 0 \; \forall \; \text{symmetric surfaces} \tag{14}$$

By integrating the solution for G over the entire particle volume, see Eq. (15), the factor γ can be obtained, which then allows to calculate the shape factor σ through Eq. (16).

$$\gamma = \frac{1}{V_p} \int_{V_p} G \, dV \tag{15}$$

$$\gamma = \frac{\sigma + 1}{\sigma + 3} \tag{16}$$

Now, using the shape factor σ and the particle volume and surface area, V_p and S_p, the diffusion length can be calculated according to Eq. (17).

$$L_{\text{diff}} = (\sigma + 1) \frac{V_p}{S_p} \tag{17}$$

The dimensionless coordinate $\tilde{r}$ is calculated from the dimensional radial coordinate and the diffusion length, as shown in Eq. (18).

$$\tilde{r} = \frac{r}{L_{\text{diff}}} \tag{18}$$

Species and energy are balanced in the same way as for the ∞ Ring model, however while the latter assumes a shape factor of 1, the GCγ model works with the shape specific factor σ, as shown in Eqs. (19) and (20).

$$\frac{\partial N_i}{\partial r} + \frac{\sigma}{r} N_i = \sum (\nu_{i,j} \; r_j) \tag{19}$$

$$\lambda \frac{\partial^2 T}{\partial r^2} + \lambda \frac{\sigma}{r} \frac{\partial T}{\partial r} = \frac{\partial (h_i N_i)}{\partial r} + \frac{\sigma}{r} h_i N_i \tag{20}$$

Since the GCγ model considers a representative cylinder, it applies a Robin boundary condition at the cylinder surface, but assumes symmetry and applies a zero gradient boundary condition at the particle centre. Boundary conditions for mass and energy balance are summarised in Eqs. (21) and (22).

$$N_i = \begin{cases} 0 & \text{for } r = 0 \\ \beta \left(c_i - c_{i,\text{bulk}} \right) & \text{for } r = 1 \end{cases} \tag{21}$$

$$\lambda \frac{\partial T}{\partial r} = \begin{cases} 0 & \text{for } r = 0 \\ \alpha \left(T_{\text{bulk}} - T \right) & \text{for } r = 1 \end{cases} \tag{22}$$

2.3. Governing equations CFD model

At the basis of the CFD code are the four steady state conservation equations for a fluid phase (continuity, species mass, momentum and energy) (Lecheler, 2014; Siemens Digital Industries Software, 2020). The continuity equation, may be written as shown in Eq. (23).

$$\nabla \cdot (\rho \mathbf{u}) = 0 \tag{23}$$

Where ρ is the fluid density, and $\mathbf{u}$ the velocity vector. A conservation equation is solved for each species. With w_i being the species mass fraction and $\mathbf{j}_i$ as the diffusive flux, the species conservation is given in Eq. (24).

$$\nabla \cdot (\rho \mathbf{u} w_i) = \nabla \cdot \mathbf{j}_i + S_i \tag{24}$$

Eq. (25) gives the momentum conservation.

$$\nabla \cdot (\rho \mathbf{u} \times \mathbf{u}) = -\nabla \cdot (\delta p) + \nabla \cdot \boldsymbol{\tau} \tag{25}$$

Here, δ is the Kronecker delta, p is the static pressure, $\boldsymbol{\tau}$ is the viscous stress tensor. For a Newtonian fluid the viscous stress tensor can be formulated as:

$$\boldsymbol{\tau} = \mu (\nabla \mathbf{u} + (\nabla \mathbf{u})^T) - \frac{2}{3} \mu \nabla \cdot \mathbf{u} \tag{26}$$

where μ is the fluid viscosity. The conservation of energy gives rise to Eq. (27).

$$\nabla \cdot (\rho E \mathbf{u}) = \nabla \cdot (\mathbf{u} \cdot \boldsymbol{\tau}) - \nabla \cdot (\mathbf{u} \delta p) - \nabla \cdot \mathbf{q} + S_E \tag{27}$$

where E is the total mass specific energy, $\mathbf{q}$ is the heat flux and S considers energy sources such as the heat of reaction.

Turbulence was modelled using a Reynolds averaged Navier Stokes (RANS) approximation, which divides all solution variables ϕ into a mean $\overline{\phi}$ and a fluctuating component ϕ'. Inserting the decomposed variables into the governing equations (23) (25) and (27), yields the following expressions:

$$\nabla \cdot (\rho \overline{\mathbf{u}}) = 0 \tag{28}$$

$$\nabla \cdot (\rho \overline{\mathbf{u}} w_i) = \nabla \cdot \mathbf{j}_i + \overline{S}_i \tag{29}$$

$$\nabla \cdot (\rho \overline{\mathbf{u}} \times \overline{\mathbf{u}}) = -\nabla \cdot (\delta \overline{p}) + \nabla \cdot (\overline{\boldsymbol{\tau}} + \boldsymbol{\tau}_{\text{RANS}}) \tag{30}$$

$$\nabla \cdot (\rho \overline{E} \overline{\mathbf{u}}) = \nabla \cdot \overline{\mathbf{u}} (\overline{\boldsymbol{\tau}} + \boldsymbol{\tau}_{\text{RANS}}) - \nabla \cdot (\overline{\mathbf{u}} \delta \overline{p}) - \nabla \cdot \overline{\mathbf{q}} + \overline{S}_E \tag{31}$$

In Eqs. (30) and (31) and additional term was introduced. $\boldsymbol{\tau}_{\text{RANS}}$ is a stress tensor, which accounts for the fluctuating component of the velocity.

$$\boldsymbol{\tau}_{\text{RANS}} = -\rho \left(\overline{u'} \left(\overline{u'} \right)^T \right) + \frac{2}{3} \rho \kappa \delta \tag{32}$$

Here, κ is the turbulent kinetic energy. The two layer κ ϵ turbulence model was used, where the Boussinesq approximation models $\boldsymbol{\tau}_{\text{RANS}}$ according to Eq. (33).

$$\boldsymbol{\tau}_{\text{RANS}} = \mu_t \left(\nabla \overline{\boldsymbol{u}} + \nabla \overline{\boldsymbol{u}}^T \right) + \frac{2}{3} \left(\mu_t \nabla \cdot \overline{\boldsymbol{u}} \right) \delta \tag{33}$$

μ_t, the turbulent eddy viscosity, is calculated according to Eq. (34), where C_μ is a model coefficient, f_μ is a damping function and t_{turb} is the turbulent time scale (Siemens Digital Industries Software, 2020; Lecheler, 2014).

$$\mu_t = \rho C_\mu f_\mu \kappa t_{\text{turb}} \tag{34}$$

The chemical reaction was implemented as a source term in the species conservation equation (24). Using the stoichiometric factor for species i in reaction j $\nu_{i,j}$, the reaction rate r_j and the catalyst density ρ_{cat}, a source term S_i for each species was calculated.

$$S_i = \sum^j (\nu_{i,j} \; r_j) \; \rho_{\text{cat}} \tag{35}$$

The energy source term S_E in Eq. (36) was implemented as a source term S in the energy balance equation (27), using the heat of reaction $\Delta_R H_j$ for reaction j and the respective reaction rate.

$$S_E = \sum^j (-\Delta_R H_j \; r_j) \; \rho_{\text{cat}} \tag{36}$$

The conjugated heat and mass transfer model, published by Kutscherauer et al. (2023) was implemented to couple the surrounding fluid phase to the porous solid particle. The solution of the fluid and solid domain are computed iteratively in parallel but separately from each other following the partitioned approach. To couple the domains the boundary conditions for energy and species mass transport at the shared fluid solid interface are calculated as a function of quantities stored in the interface nearest cell centroid of the fluid and solid side. These boundary conditions are updated continuously during the iteration procedure until convergence is reached. The authors refer the reader to the original publication for the salient features of this model.
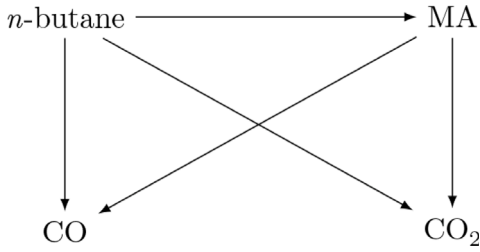
Fig. 3. Simplified four-species-five-reaction reaction network for the selective oxidation of *n*-butane to MA (adapted from (Müller et al., 2021)).

2.4. Reaction kinetics

To calculate the species source terms, rates for all considered reactions need to be determined first. Stationary reaction kinetics for the selective oxidation of *n* butane to MA, published by Müller et al. (2021), were implemented to calculate the reaction rates. These kinetics describe the MA synthesis with five reactions, according to the reaction network shown in Fig. 3, by assuming a Mars van Krevelen type rate law. A reaction rate is calculated for each of the five considered reactions. The authors refer the reader to the original publication by Müller et al. (2021) for further details on the reaction kinetic model.

3. Grid and domain independence

3.1. Domain independence

To study the effect different flow conditions have on a catalyst particle, one wants to exclude any influences on the flow other than the particle itself. Ideally, this would mean placing a sphere in a domain of infinite size. As CFD simulations require a finite domain however, it must be ensured that the domain confining boundaries do not exhibit any effect on the flow. The initial domain size was chosen to be $15 \times 15 \times 20$ (Height × Width × Length) particle diameters d_p, in accordance with results from Dixon et al. (2011). To determine domain independence, the halved and a doubled domain size were also tested. Fluid flow, entering the domain with a temperature of 300 K, around a spherical particle with a temperature of 330 K, at a Reynolds number of $Re_p = 1000$ was simulated. The Nusselt number Nu and drag coefficient C_D were observed to assess the influence on the heat transfer and flow behaviour, respectively. Tested domain sizes and results are given in Table 2. All domains where meshed with identical settings. A cell size of $d_p/10$ was chosen, with refinements in the wake region ($d_p/20$) and on the particle surface ($d_p/100$). Prism layers were created on the particle surface with a thickness corresponding to the momentum boundary layer thickness. Ten prism layers with a stretching factor of 1.1 were chosen. The momentum and thermal boundary layer thickness ι and ι_t were calculated according to Eqs. (37) and (38), respectively (Dhole et al., 2006).

$$\iota = \frac{1.13}{Re^{0.5}} \tag{37}$$

$$\iota_t = Pr^{-0.33} \, \iota \tag{38}$$

This way, it was ensured that the first prism layer would not exceed the size of either boundary layer in any of the cases considered in this study. Accordingly, sufficiently low y^+ values ensued ($y^+ \ll 1$), necessary for the two layer approach of the $\kappa - \epsilon$ turbulence model (Siemens PLM, 2022).

It was found that, compared to the initial domain, the doubled domain produced results within 0.18% and 0.66% for Nu and C_D, respectively. These findings are in good agreement with (Dixon et al., 2011), who found an error < 1 % for C_D and < 0.25% for Nu. Meanwhile, the halved domain showed deviations in the size of 0.94%

Table 2
Results for the domain independence study. Spherical particle at $Re_p = 1000$.

Domain size	Nu	C_D
–	–	–
$7.5 \times 7.5 \times 10$	19.22	0.56
$15 \times 15 \times 20$	19.04	0.54
$30 \times 30 \times 40$	19.01	0.54

Table 3
Results of mesh independence study.

Cell size mm	Cell count –	Nu –	Error %	C_D –	Error %
1	559 291	19.19	1.56	0.53	3.75
0.5	2 179 183	19.04	0.78	0.54	1.31
0.25	9 685 486	18.93	0.18	0.54	0.29
∞^{-1}		18.89		0.55	

and 3.73%. Considering the increase in cell count and subsequently the increase in compute time along with an error of less than 1 % compared to the extrapolated, infinitely resolved solution for both flow and heat transfer, it was opted to keep the initial domain size for the remainder of this study.

3.2. Grid independence

For the mesh independence study, a Grid Convergence Index (GCI) approach, based on the Richardson extrapolation, was used (Roache, 1998). The Richardson extrapolation determines the "true" value of a field variable ϕ, such as the average temperature in the particle for example, by extrapolating from the value obtained by a medium (m) sized and a fine (f) mesh. The "true" value in this case corresponds to the value that would be obtained from an infinitely fine (∞) mesh (M.Moghaddam et al., 2021). A refinement factor r_g is calculated from the cell count N of both meshes (see Eq. (39)). With an assumed convergence rate $p = 2$, the value of the field variable obtained from an infinitely fine mesh ϕ_∞ can be calculated from Eq. (40). From this value, the relative error E associated with each mesh size can be determined through Eq. (41) (Roache, 1998).

$$r_g = \sqrt{\frac{N_f}{N_m}} \tag{39}$$

$$\phi_\infty = \phi_f + \frac{\phi_f - \phi_m}{r_g^p - 1} \tag{40}$$

$$E = \left| \frac{\phi_\infty - \phi_f}{\phi_\infty} \right| \tag{41}$$

Three levels of mesh refinement were investigated in a manner analogous to the domain independence study. Mesh settings described in the domain independence study were used as the medium size mesh, while for the coarse mesh the cell size was doubled and for the fine mesh the cell size was halved. Prism layers around the particle were excluded from cell size changes such that they would still resolve the boundary layers, independent of the level of mesh refinement. Results of the mesh independence study are shown in Table 3.

Deviations from the "true" value are marginal for all three mesh sizes, and each refinement level would yield acceptable results in principle. However, it becomes apparent that improvement of accuracy between the coarse and medium mesh exists, especially the flow the error reduces substantially (1.31 < 3.75). In a trade off between increased accuracy and computation time, again the medium mesh was chosen for further simulation work.
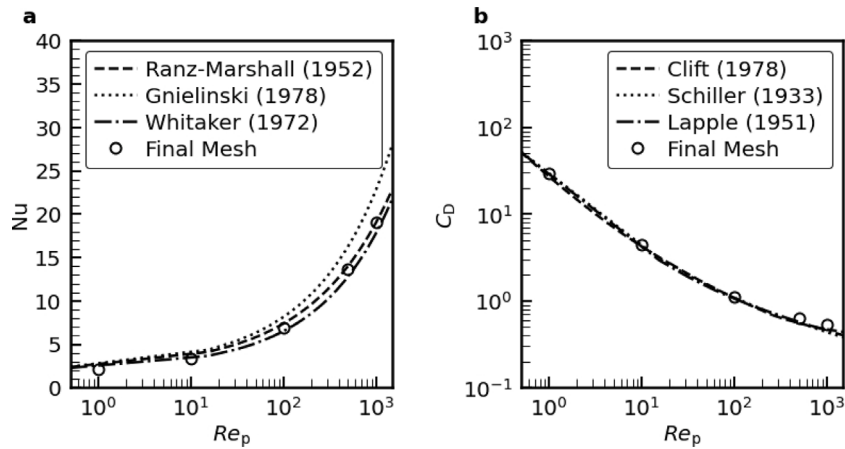
Fig. 4. Validation of the final mesh iteration by Nusselt number Nu and drag coefficient C_D for a range of Reynolds particle numbers Re_p (Ranz and Marshall, 1952; Gnielinski, 1978; Whitaker, 1972).

3.3. Validation

Domain and grid independence were established only for turbulent flow at $Re_p = 1000$. Dhole et al. (2006) found that laminar flow at lower Re_p generally required larger domains than turbulent flow. To establish whether the previously generated mesh is valid for different flow conditions, simulations across the range of investigated Re_p (1 1000) were carried out. Again, Nu was observed for heat transfer and C_D for flow behaviour. Simulation results were compared against different correlations from the literature (Ranz and Marshall, 1952; Gnielinski, 1978, 1982; Whitaker, 1972; Clift et al., 2005) in Fig. 4. It becomes readily apparent that the simulation results fit very well within the range of correlations. On this basis it was decided that the mesh was fit for use within the range of $1 < Re_p < 1000$.

4. Results

First, results of the CFD simulation are presented in the form of in traparticle profiles for both n butane partial pressure and temperature. Results are shown for four different inclination angles under inlet and hot spot conditions. In a second step, the 3D CFD results are compared to two different one dimensional models, to assess to which degree the 1D formulation can describe a 3D particle. Finally, the CFD simulations are manipulated so that the simplifying assumptions of the 1D models are exactly fulfilled and once again compared to the 1D results.

4.1. CFD results

Fig. 5 shows n butane partial pressure and temperature profiles for a ring shaped particle at different inclination angles. The data shown are axially and tangentially averaged at each point in the radial direction The radial domain spans from $\tilde{r} = 0$, which represents the inner radius of the ring, to $\tilde{r} = 1$, which is at the outer radius of the ring. Fig. 5a d show the n butane partial pressure profiles under inlet conditions for 0°, 30°, 60° and 90°. For 0° the values at the inner and outer surface are 1,437 Pa and 1,455 Pa, respectively. While 30° and 60° experience similar surface values, at 90° the inner surface has a much lower n butane partial pressure than on the outer surface, (947 Pa and 1,461 Pa respectively). At an inclination angle of 0°, the inner channel is directly opened to the external flow, which results in good convective transport from the bulk fluid to the inner surface of the particle   hence the species partial pressures are similar for both the inside ($\tilde{r} = 0$) and outside ($\tilde{r} = 1$) surface. With increasing inclination angle, the ring is turned away from the direction of the external flow field, decreasing the accessibility of the inner channel to convective transport and thereby lowering the n butane partial pressure on the inside surface ($\tilde{r} = 0$).

Table 4

Heat- and mass transfer coefficients for inlet and hot-spot conditions, extracted from correlations by Gnielinski (1975) and CFD simulations.

	α W m^{-2} K^{-1}	Nu	$\beta_{C_4H_{10}}$ m s^{-1}	$Sh_{C_4H_{10}}$
Inlet conditions				
CFD (0°)	37.98	9.83	0.031	5.06
CFD (30°)	42.89	11.14	0.035	5.66
CFD (60°)	42.44	11.02	0.033	5.38
CFD (90°)	38.31	9.95	0.017	2.78
Gnielinski	50.38	13.02	0.023	3.75
Whitaker	38.36	9.92	0.046	7.38
Hot-spot conditions				
CFD (0°)	37.42	9.76	0.039	5.48
CFD (30°)	42.37	11.04	0.043	6.02
CFD (60°)	41.93	10.93	0.041	5.74
CFD (90°)	38.01	9.91	0.025	3.46
Gnielinski	50.38	13.04	0.026	3.72
Whitaker	38.39	9.94	0.051	7.21

This phenomenon can also be seen in Fig. 6. In all cases, the n butane partial pressure drops to approximately 500 Pa in the particle centre. The corresponding temperature profiles are shown in Fig. 5e h with reference to the bulk temperature T_{bulk}. At an inclination angle of 0° the particle experiences the highest temperature difference to the bulk, with values of 27.8 K and 27.2 K at the inner and outer surface. The next highest temperature can be found at an angle of 90°, whilst at 30° and 60° the temperature is approximately 4 K lower than at 0°. It can be seen that with increasing inclination angle the inner surface temperature rises compared to the outer surface, reaching the highest difference at 90° with 25.2 K and 23.7 K. This can be again attributed to the increasing obstruction of the inner channel with increasing inclination angle. The temperature profiles show little temperature increase within the particle, such that the particles almost become isothermal.

Fig. 5i l show the n butane partial pressure profiles and Fig. 5m p the corresponding temperature profiles under hot spot conditions. Overall, the observed trends are similar to inlet conditions with asym metry of profiles increasing with inclination angle and highest intra particle temperatures observed for 0° with the exception that at 90° the intraparticle temperature does not exceed the temperature observed at 30° and 60°. Noticeably, the n butane profiles have become broader compared to Fig. 5a d, advertising that the majority of the chemical reaction takes place in the outer layers of the catalyst particle. This is a consequence of the rate of reaction increasing more strongly with respect to temperature than the mass transport.
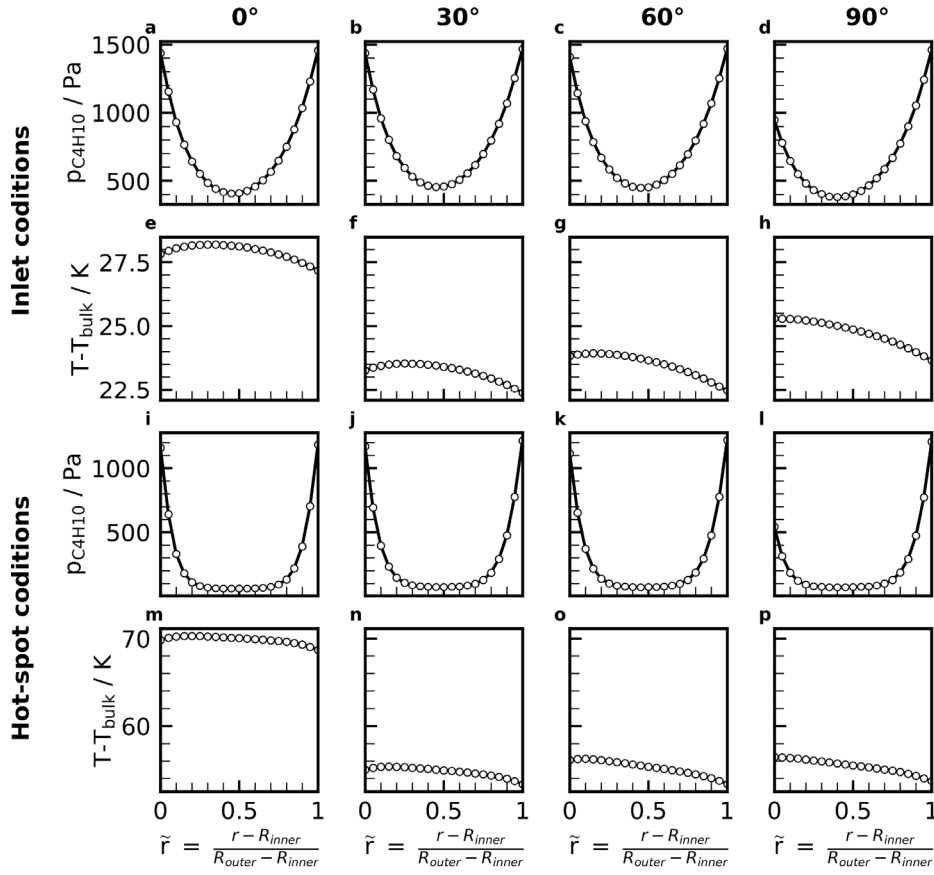
Fig. 5. Intraparticle profiles are shown for inlet (a–h) and hot-spot (i–p) conditions. Distinct minima in the n-butane partial pressure profiles (a–d and i–l) highlight the internal mass transport limitation, whereas the temperature profiles (e–h and m–p) display signs of external heat transport limitation.

Overall, distinct minima occur in the n butane partial pressure profiles. Especially under hot spot conditions a strong limitation in intraparticle diffusion dominates the mass transfer, as evidenced by the rapid decrease of $p_{C_4H_{10}}$ to zero. For 0° inclination angle (Fig. 6a, i), 90% of n butane conversion takes place in the first 708 μm and 342 μm from the outer surface of the particle, for inlet and hot spot conditions respectively. On the other hand, the temperature profiles show that the particles experience temperatures that are considerably higher than in the fluid bulk, while at the same time the temperature increase within the particle is minor. This is a good indication of an external transport limitation. Both can be verified by comparing the resistances for external and internal transfer processes, Ω_{int} and Ω_{ext}. External and internal mass transport limitations are calculated corresponding to Eqs. (42) (45), using the transport coefficients values according to Whitaker (1972) (see Table 4) and volume averaged values for the n butane effective diffusivity.

$$\Omega_{ext,heat} = \frac{1}{\alpha 2\pi R_{outer} H} \tag{42}$$

$$\Omega_{int,heat} = \frac{ln\left(\frac{R_{outer}}{R_{inner}}\right)}{\lambda 2\pi H} \tag{43}$$

$$\Omega_{ext,mass} = \frac{1}{\beta_{C_4H_{10}} 2\pi R_{outer} H} \tag{44}$$

$$\Omega_{int,mass} = \frac{ln\left(\frac{R_{outer}}{R_{inner}}\right)}{D_{eff,C_4H_{10}} 2\pi H} \tag{45}$$

For inlet conditions, the internal heat transfer resistance is calculated to be $49.81\,\mathrm{K\,W^{-1}}$, whereas the external transfer resistance is $232.79\,\mathrm{K\,W^{-1}}$. The internal mass transfer resistance is calculated to be $1.94 \times 10^7\,\mathrm{s\,m^{-3}}$, whereas the external transfer resistance is

$2.82 \times 10^5\,\mathrm{s\,m^{-3}}$. The ratio of both heat and mass transfer coefficients confirms that heat transfer is externally limited whereas the mass transport is limited by pore diffusion. In good agreement with these observations, Carberry (1966) reported that in heterogeneous catalysis the largest temperature gradient will generally be found in the gas phase boundary layer surrounding the particle, whereas the largest concentration gradient usually occurs within the particle. Gao et al. (2021) reported that the VPO catalyst pore network undergoes structural change during operation, where initially present nanoporous structures transition to micrometer sized mesopores. Change of the pore network structure will undoubtedly impact the intraparticle profiles for both species partial pressures as well as temperature. In the presented stationary simulations, only a mean pore diameter is considered, which was extracted from measurements on the pristine catalyst.

What has previously been hypothesised on the basis of Fig. 5, where the obstruction of the inner channel with increasing inclination angle leads to lower n butane partial pressures and higher temperatures on the inside surface of the particle, is now visualised in Figs. 6 and 7. Fig. 6 shows the temperature (a d) and velocity scenes (e h) under inlet conditions for the different inclination angles and Fig. 7 shows transport coefficients for heat (α, b) and n butane ($\beta_{C_4H_{10}}$, c) for each surface of the particle individually. While there is almost bulk velocity in the channel of the particle at 0°, it reduces with increasing inclination angle (30° and 60°) due to flow restriction until a stagnant zone is formed at 90°. This influences the convective heat transport, as can be seen in Fig. 6d, where the temperature in the channel is noticeably higher compared to the bulk.

This effect of flow on heat and mass transport can also be seen in figure Fig. 7, where for 0° the upstream surface has the highest rate of heat and mass transport. In contrast, the downstream surface lies in the shadow zone of flow, where the formation of a recirculating vortex
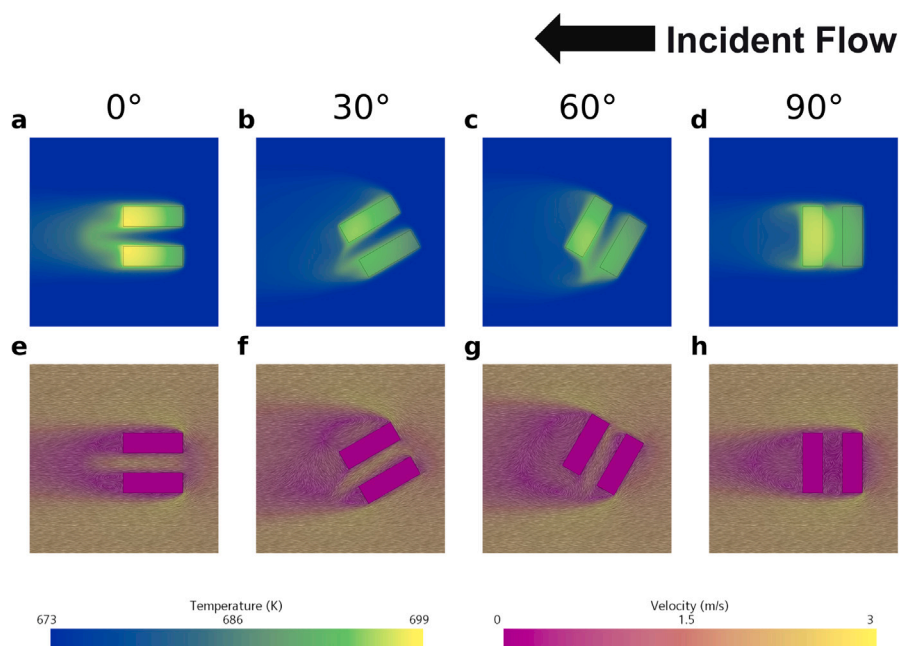
Incident Flow

Fig. 6. Temperature (a–d) and velocity (e–h) scenes under inlet conditions, taken through the centre of the catalyst particle for different inclination angles.
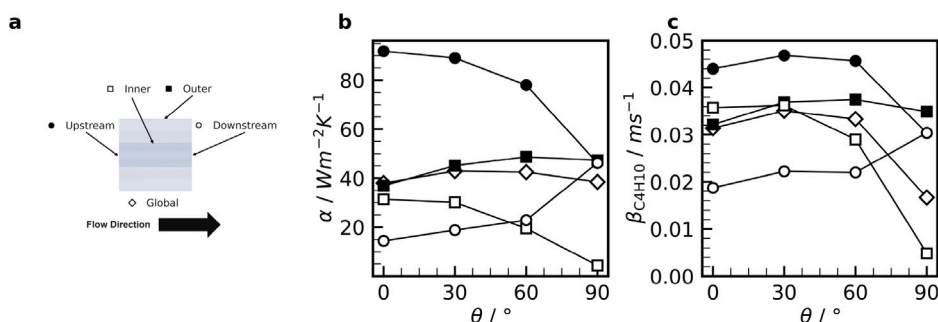

Fig. 7. Individual surfaces (a), Heat- (b) and mass (c) transport coefficients α and $\beta_{C_4H_{10}}$ for each surface of the particle under inlet conditions. Transport coefficients are plotted over the inclination angle θ.

causes backmixing and large boundary layers, which are detrimental for heat and mass transfer between the particle and the bulk fluid. Hence, the downstream surface transport coefficients are dramatically lower compared to the upstream surface. Inside the inner channel, the flow is slightly accelerated after it has passed through the stagnation point in front of the particle. Within the channel the fluid travels at bulk velocity, and correspondingly the transport coefficients for the inner surface are of similar magnitude to the outside surface, which of course also experiences bulk velocity. After passing through the inner channel, the fluid mixes with the low velocity shadow zone behind the particle and accelerates some of the surrounding fluid, causing a jet like appearance. As the particle is rotated, the low velocity shadow zone behind the particle forms less on the downstream surface, and more on the outer surface (compare Fig. 6e h). Therefore, with further rotation of the particle the upstream surface transport coefficients decreases whilst the downstream surface coefficients increases until at an angle of 90° they coincide at identical values, since they take in symmetrically identical positions relative to the surrounding flow field. The outside surface transport coefficients slightly increase with inclination angle as it turns from being parallel aligned to the flow to a perpendicular alignment, meanwhile the inside surface values for α and $\beta_{chC4H10}$ decrease as the flow restriction through the channel is advanced, thus decreasing the amount of convective transport as well, until reaching minimum values close to zero at 90°. Analogous observations were made under hot spot conditions, the corresponding temperature and

velocity scenes as well as the transport coefficient plots can be found in the supporting information.

Fig. 7 makes evident how the global α is highest for 30° and 60°, while it is slightly lower for 0° and 90° under inlet conditions. Simultaneously, the global $\beta_{C_4H_{10}}$ is much lower for 90° than for 0°, 30° and 60°. A combination of comparably low heat transfer with good mass transfer results in 0° exhibiting the highest intraparticle temperatures due to sufficient supply of reactants paired with poorer removal of heat. An inclination angle of 90° leads to a similarly low heat transfer coefficient as at 0° but a much worse mass transfer coefficient $\beta_{C_4H_{10}}$. Therefore, heat removal is similar as at 0°, but the amount of heat released is limited by the supply of reactants, ensuing in lower intraparticle temperatures compared to 0°. Since the angles 30° and 60° manifest the highest values of α, they experience lower intraparticle temperatures.

In light of the previous results, the reduced n butane partial pressure and the increased temperatures at the inner surface for an inclination angle of 90°, shown in Fig. 5, can be attributed to the accessibility of the different surfaces for heat and mass transport. The almost equal values for surface temperature and n butane partial pressures shown in Fig. 5a, e, i, m (0°) are a result of α and $\beta_{C_4H_{10}}$ values of similar magnitude. With increasing inclination angle the divergence of surface transport values becomes more pronounced, as a consequence of increasing deviation of transport coefficients. At 90° (Fig. 5d, h, l, p) this culminates in the strongest mismatch between inner and outer surface values, owing

to the inner surface α and $\beta_{C_4H_{10}}$ becoming almost zero. Generally in Fig. 5a d it is visible that the minima of the partial pressure profiles are slightly shifted toward the $\widetilde{r} = 0$, while in Fig. 5i l this is super posed with the strong bulbous shape, diminishing the visibility of the shift. This effect cannot be explained by a decrease in heat and mass transport from the bulk fluid phase to the inside channel of the particle, since there should not be a shift at 0° in that case. Rather, it is caused by the change of surface area over the radial domain, thereby causing an increased diffusive flux when approaching $\widetilde{r} = 0$. The aforementioned findings are in good agreement with the work of Dixon (2014), who investigated the behaviour of a single, ring shaped particle for steam methane reforming at different inclination angles. A difference arises in the behaviour of the downstream surface value, which Dixon found to decrease rather than to increase with increasing inclination angle, attributed to an increase in size of the recirculation flow downstream the cylinder. A likely explanation lies in the range of investigated Re_p numbers, which were $1000 < Re_p < 10,000$ in the study of Dixon for methane steam reforming conditions, compared to $Re_p = 400$ in our work, dictated by n butane oxidation conditions. At these significantly lower Re_p numbers, the downstream recirculation zone is much less pronounced.

4.2. Comparative analysis of 3D and 1D results

The complete description of a catalyst particle in external flow is a 3D problem, for example by fluxes in three spatial directions (axial, radial and tangential), external non uniform flow around the particle and non uniform boundary layer thickness. CFD simulations can fully resolve each dimension, whereas 1D continuum models cannot. To determine the extent to which the 1D models are able to describe the particle, even at different inclination angles, we compare the results from two different 1D models to the CFD.

In parallel to Fig. 5, Fig. 8 shows radial profiles of n butane par tial pressure and temperature. Two 1D model formulations (dashed and dotted lines) using two different correlations (Gnielinski (1975) and Whitaker (1972) shown in brown and blue, respectively) to obtain transport parameter are shown. CFD data are taken from 10,000 Monte Carlo distributed points for each CFD case and plotted transparently, so that the intensity of the colour gives information about the spatial distribution of the variable. Under inlet conditions, the n butane partial pressure (Fig. 8a d) forms parabolic trajectories. A slight distribution of data points are located between the parabolic profile and the surface values for the inside of the particle, eliciting a 'filled' appearance of the parabolic profile. These values are caused by the frontal surfaces of the particle and the surface adjacent regions. At first glance, the 1D models agree exceptionally well to the CFD data points regarding the surface values, the location and value of the minima, and the gradient of the profile. This appears to be independent of model formulation or transport correlation, despite a not insignificant deviation in mass transport coefficients β_i between the CFD, the correlation of Gnielinski, and Whitaker (compare Table 4 for reference). As previously outlined (see Section 4.1), the selective oxidation of n butane is limited by internal diffusion regarding the mass transport. Ergo, the external mass transport is not the limiting resistance and consequently plays a subordinate role in the determination of the profiles. The interplay of internal diffusion and reaction is described well by both model formulations, as evidenced by the matching n butane partial pressure profiles. A caveat to the previous statement is that the 1D models do not show the lowered partial pressures on the inner surface ($\widetilde{r} = 0$) that arise from the channel blocking at an inclination angle of 90°, a phenomenon that was extensively discussed in Section 4.1. The corresponding temperature profiles (Fig. 6e h) show that the particle experiences a wide distribution of temperatures. At an inclination angle of 0° the temperature spans between $16\,K$ and $30\,K$ above bulk temperature. The limited curvature of the CFD data points suggests that the particle is almost isothermal. A comparison with Fig. 6 confirms

that the temperature is distributed along the particle in the direction of external flow, but at each position shows very little intraparticle temperature rise. Its well visible that with increasing inclination angle the span of temperatures becomes more narrow on the inside surface ($\widetilde{r} = 0$) which again owes to the formation of a stagnant zone in the channel. The use of the Gnielinski correlation yields much lower temperatures than using the Whitaker correlation. A brief review of the α values in Table 4 reveals that calculations according to Gnielinski result in a much higher α value than extracted from the CFD, whereas calculations according to Whitaker give rise to α values that are in line with CFD results. Hence it is evident that the use of the former leads to lower temperatures. Unlike the mass transport, the heat transport is externally limited for the reaction system investigated in this work, hence the transfer coefficients play a vital role in the determination of the temperature profiles. It is also evident that the GCγ model predicts generally lower temperatures than the ∞ Ring model, which generally over predicts the temperatures by up to $5\,K$. The GCγ model fits the temperatures quite well for 30°, 60° and 90° but falls into the lower range of temperatures at 0°. Under hot spot conditions, the CFD data points form a distinctly bulbous profile for the n butane partial pressure (Fig. 8i l). The n butane partial pressure drops to zero within the outer layers of the catalyst, forming steep gradients. Datapoints between the main profile and the surface values are much reduced compared to inlet conditions, owing the rapid reduction of partial pressure also from the frontal surfaces inward the particle. The trends already described for inlet conditions remain upheld: the 1D models agree well with the CFD results but cannot describe 3D external effects such as the channel blocking induced shift in inner surface butane partial pressure at 90°. Fig. 8m p show the temperature profiles under hot spot con ditions. Again, the particles experience a temperature distribution but at each position are almost isothermal in radial direction. Due to the accelerated reaction rate at higher temperature, the catalyst particle experiences temperatures between $80\,K$ and $55\,K$ above bulk tempera ture at 0°. As under inlet conditions, increasing inclination angle leads to constriction of inner surface temperatures due to channel blocking. The correlation of Gnielinski yields lower temperatures than the CFD due to the over prediction of α. In contrast to inlet conditions, now both 1D model formulations are within range of the CFD values when using Whitaker correlation, whereas previously the ∞ Ring model slightly overpredicted the temperature profiles.

Global values for the catalyst effectiveness factor, calculated for the main reaction $C_4H_{10} \rightarrow MA$ according to Eq. (46), are shown in Fig. 9.

$$\eta_{C_4H_{10},MA} = \frac{1}{V_p} \cdot \int_{V_p} \frac{r}{r_{surf}} dV \tag{46}$$

Error bars indicate the values of catalyst effectiveness factors according to one standard deviation of the surface reaction rate.

In line with the n butane partial pressure profiles shown in Fig. 8a d and i l, under inlet conditions the catalyst effectiveness factor η lies in the vicinity of 70%, whereas the elevated temperature under hot spot conditions leads to values below 40%. Maffei et al. (2016) reported a similar effect for H_2 combustion, where the catalyst effectiveness factor decreased rapidly with temperature as a result of incipient transport limitation. A comparison of the η values extracted from the CFD for the different inclination angles shows that for 30° and 60° the catalyst effectiveness factor is slightly elevated compared to 0° and 90°. This can be explained by the slightly improved external heat transport (compare Fig. 7) for 30° and 60°, which lower the intraparticle temperatures and slow the reaction rates. Additionally, the inclination angle 90° shows a broader error bar than the other angles, which can be attributed to the channel blocking. The stagnant zone causes increased temperature and reduced n butane partial pressure and therefore much different reaction conditions compared to the outer surface, which increases the global surface standard deviation. Because of the elevated reaction rates at higher temperature, as well as the generally lower catalyst effectiveness factor, the broadened error bar cannot be seen for an inclination angle of 90° under hot spot conditions.
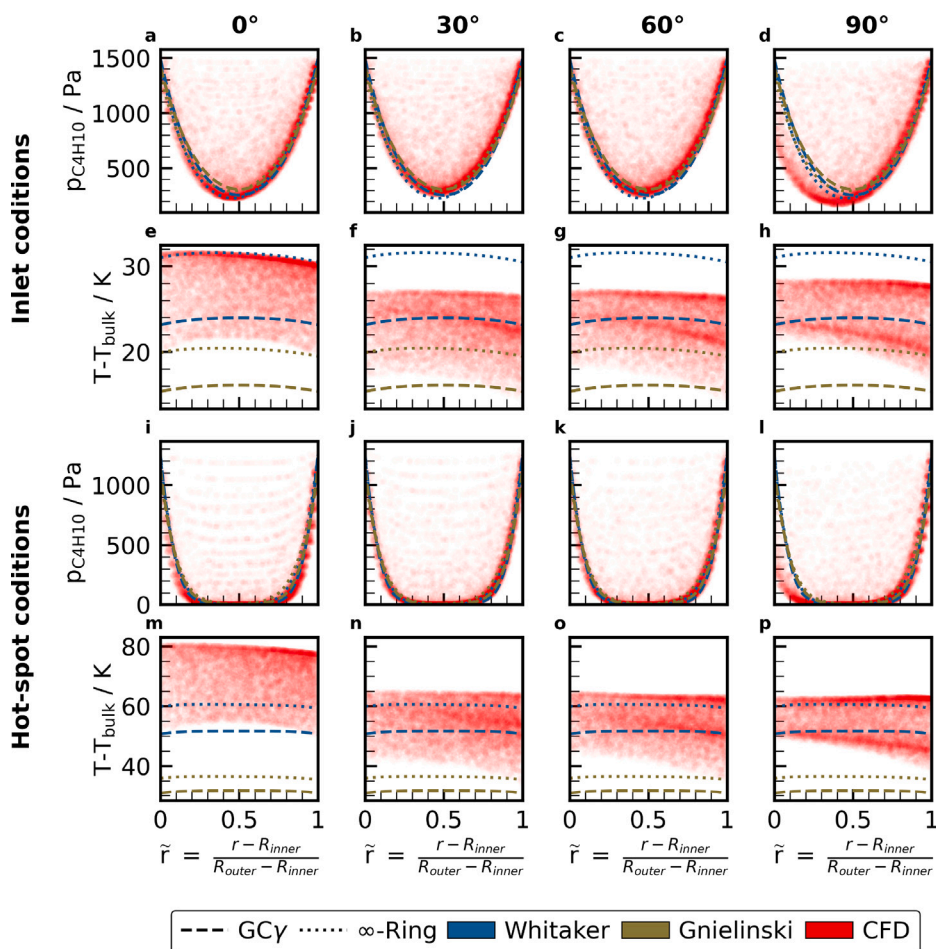
Fig. 8. Overview of intraparticle profiles under inlet (a–h) and hot-spot conditions (i–p). *n*-Butane (a–d and i–l) and temperature (e–h and m–p) profiles are compared between 1D models and the 3D CFD. Two different 1D model formulations were employed, using two different transport correlations (Whitaker, 1972; Gnielinski, 1975).
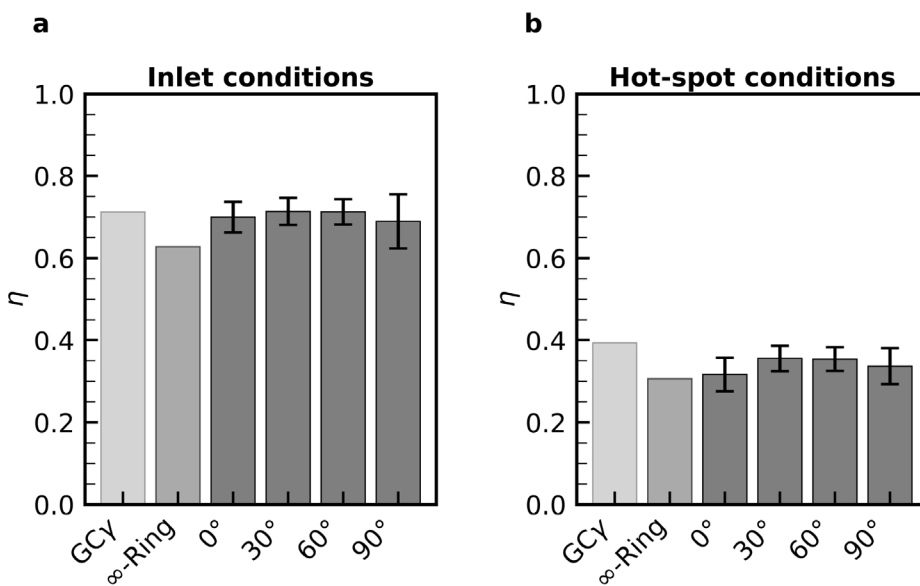

Fig. 9. Catalyst effectiveness factor η under inlet (a) and hot-spot (b) conditions for the 1D models and for the different inclination angles via CFD simulation. Error bars indicate the standard deviation via the surface concentration.

Table 4 summarises the Nusselt and Sherwood numbers as well as the respective transport coefficients α and β_{C4H10} calculated according to Gnielinski (1975) and Whitaker (1972) as well as the values extracted from the CFD simulations. As briefly mentioned in the previous
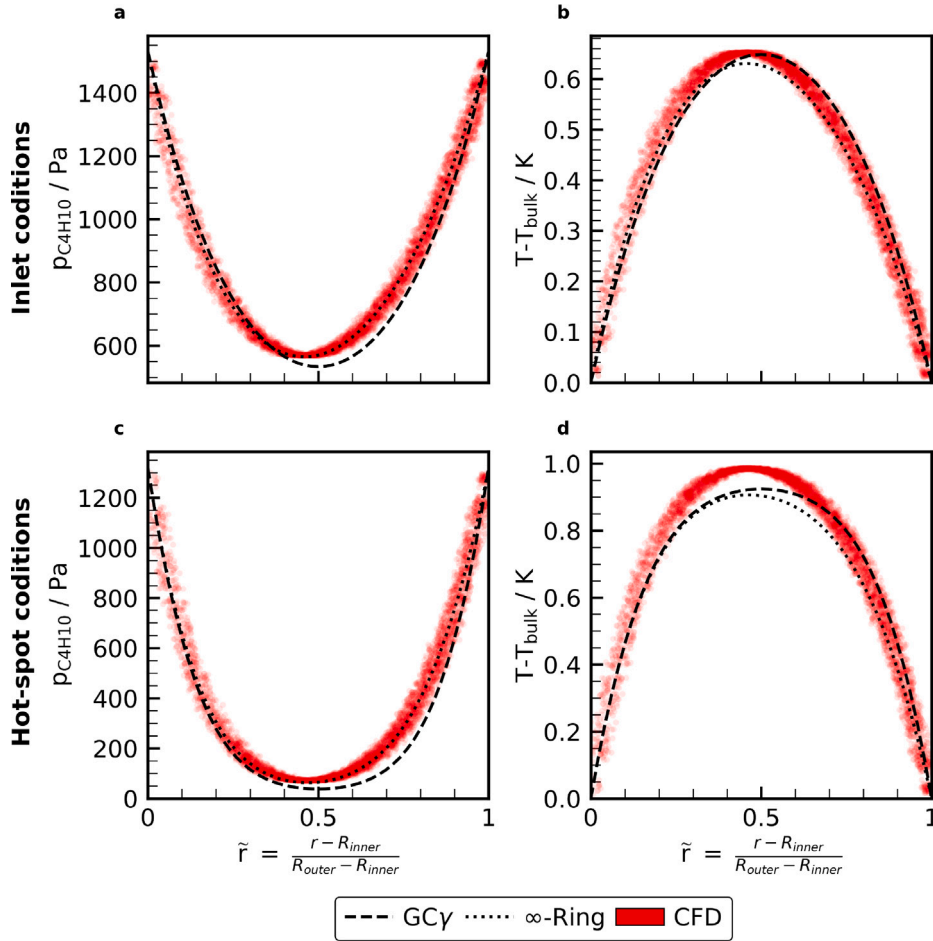
Fig. 10. Comparison of a 3D infinite ring with 1D model formulations under inlet (a–b) and hot-spot (c–d) conditions, via temperature and *n*-butane partial pressure profiles.

paragraphs, the values in Table 4 are in good agreement with the comparison between 1D models and 3D CFD, and with the observation that the 1D models give rise to temperature profiles within reasonable range of the CFD data points only when using the correlation by Whitaker. At this point it shall be pointed out that Whitaker reported deviations between experimental measurements and his correlation by up to 25% for cylindrical and up to 30% for spherical particles. Further it has to be noted that the Schmidt numbers Sc (0.21 – 0.46) are slightly below the range for which either of the correlations were validated ($0.7 < Sc < 70,000$ (Gnielinski, 1975) and $0.67 < Sc < 300$ (Whitaker, 1972)). Despite the fact that the values for α calculated according to Gnielinski deviate somewhat from the CFD results and the Whitaker correlation, they are still well within the accepted range of accuracy of transport correlations.

In summary, both 1D model formulations were able to describe the *n* butane partial pressure profiles remarkably well, whereas temperature profiles were predicted slightly different. These discrepancies likely arise as a result of the major simplifications of the 1D model, where the entire particle is treated with a single boundary condition for each surface, and axial fluxes induced by the frontal faces are neglected. The overall heat transfer is dominated by the external heat transfer, which is implemented via a Robin boundary condition in the 1D model formulations (see Section 2). However, the particle does not experience one singular boundary condition (e.g. a fixed temperature, concentration or a flux) but rather a wide distribution of the concerned variable over its surface. As the 1D model can only define a singular

boundary condition per surface, it is inherently unable to describe the wide variation of boundary values that the 3D particle experiences. When a case arises where the boundary conditions are the determining factor, then this can easily manifest in deviations compared to the 3D case. Nevertheless, when choosing the boundary conditions carefully, accurate temperature profiles can be obtained, such as in the above cases when using the Whitaker correlation. In contrast, the mass transport is insensitive to the boundary conditions due to its internal diffusion limitation, as evidenced by the production of almost identical profiles despite rather different values for β_i. Considering the respective limiting resistances, it becomes apparent why the 1D *n* butane partial pressure profiles match the CFD data points almost perfectly in Fig. 8 while the temperature profiles do not. Some publications suggest that estimation of transport parameters in continuum modelling leads to errors, since they are derived from measurements that do not consider chemical reaction (Wijngaarden and Westerterp, 1993; Marx, 2012; Lesser, 2016). Our results disagree with this suggestion since transport parameters estimated through engineering correlations closely matched results obtained from our CFD simulations. It must be emphasised however that the aforementioned studies considered entire fixed bed reactors rather than single catalyst particles. Resolving the particle in only 1D leads to neglect of the axial direction. In a 3D particle however, the frontal surfaces are available for mass and heat flux as well. As a result, the particle experiences fluxes not only in the radial, but also in the axial and tangential direction as well, which cannot be resolved when considering only a single dimension. In summary, both
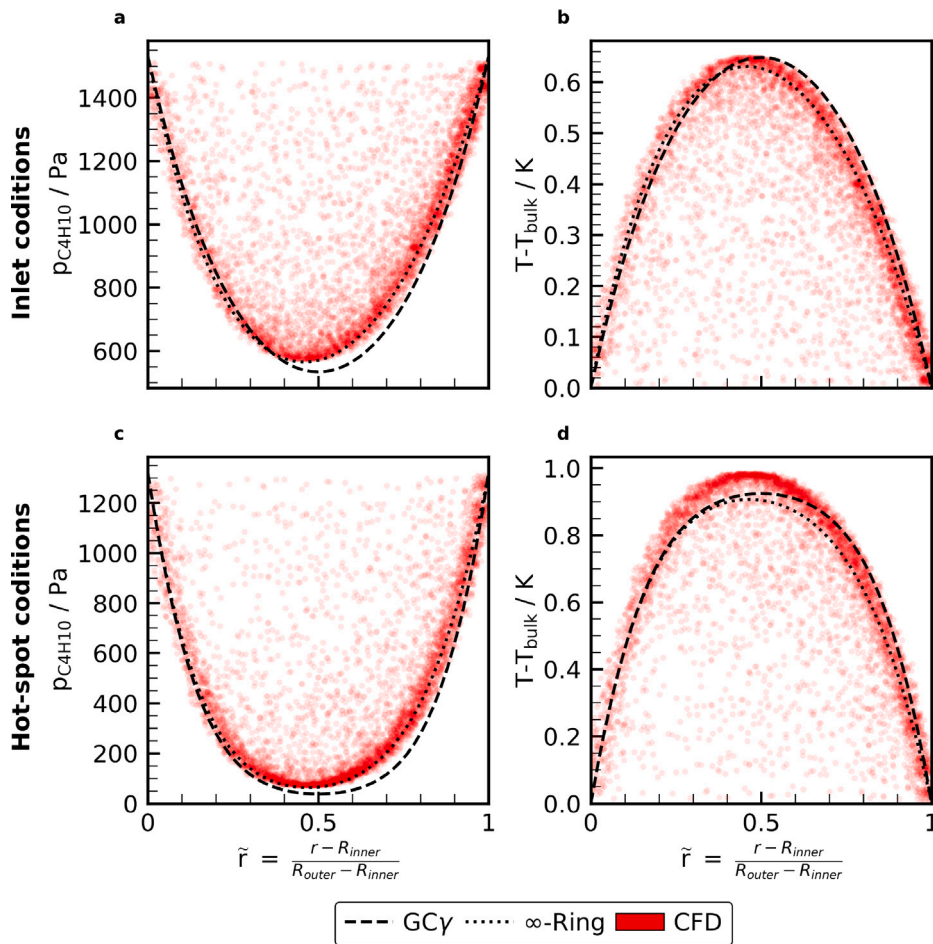
Fig. 11. Temperature and *n*-butane partial pressure profiles under inlet (a–b) and hot-spot (c–d) conditions. Considering the frontal surfaces leads to axial fluxes in the particle, creating deviations of the 3D case to the 1D model results.

model formulations can describe the 3D case remarkably well, albeit phenomena such as the channel blocking cannot be easily reproduced. However, it is conceivable to manipulate the inner surface transport coefficients in a manner that allows to describe even that. Both the feasibility and purpose of this practice are questionable however, when considering an entire fixed bed. Besides the individual profiles the 1D model formulations were also able to describe the catalyst effectiveness factor η, a global variable, with acceptable accuracy for the case of a single catalyst particle.

4.3. Idealised 3D cases

In order to investigate whether the wide range of values on the particle surface does cause model error, three dimensional simulations for an idealised ring were compared with the 1D models. We hypothesise that a replication of the theoretical infinite ring with homogeneous boundary conditions will lead to exactly coinciding 1D and 3D profiles. Therefore, we considered the catalyst particle only, neglecting the surrounding fluid phase, and implemented fixed temperature and mass fraction boundary conditions. A zero flux condition was placed on the frontal surfaces to emulate an infinitely long ring, thereby exactly corresponding to the underlying assumption of the ∞ Ring model. Fig. 10 shows the *n* butane partial pressure (a, c) and temperature (b, d) profiles under both inlet and hot spot conditions. CFD data points

were extracted and plotted similar to Fig. 8, the two different model formulations are distinguished by the line style. Surface temperature and concentration are applied as Dirichlet boundary condition, hence no transport correlations appear. The 3D data indicates parabolic profiles for partial pressure and temperature, with partial pressure decreasing and temperature increasing in the particle. In line with previous results, the maximum intraparticle overheating is below 1 K, therefore the particles are once again almost isothermal. Under hot spot conditions the reaction is accelerated, causing lower partial pressure values and higher temperatures compared to inlet conditions. The 3D data indicate that the minima and maxima are not exactly at the centre of the particle, but are shifted towards the inner surface (left in the plots). As previously explained, this is an entirely geometrical phenomenon. As the ∞ Ring model considers a ring shaped particle, it is able to describe this shift very well. The GCγ model in contrast considers a representative cylindrical particle and applies a symmetry condition at the centre, thereby it is intrinsically unable to describe the shift in minima/maxima. Regardless of this shortcoming, which frankly in practice is negligible for the case considered in this work, both model formulations do coincide perfectly with the CFD results, confirming our previously postulated hypothesis.

In Fig. 10 no data points appear in the area between the surface values and the parabolic profile in the inside of the catalyst particle, such as can be seen in Fig. 5. As stated in the previous section, these values stem from the frontal surfaces and the fluxes through them.

Therefore, the 3D infinite cylinder was again modified so that mass and heat flux through the frontal area were allowed. The resulting profiles are shown in Fig. 11. At first glance we can now see the previously absent data points in the aforementioned area, thereby proving that they are the product of frontal surfaces inducing axial fluxes in the particle. Due to the axial fluxes, the 3D cylinder cannot simply be reduced to a 1D problem any longer without loss of information, as evident from Fig. 11. Nevertheless, both simplified 1D models are able to describe the average radial profiles to a satisfactory degree.

5. Conclusion

In this study, the capability of 1D continuum models to describe the selective oxidation of n butane on the particle scale was assessed. Single particle simulations including chemical reaction were conducted for two different 1D model formulations and for a 3D CFD model. Results were compared with regard to global (catalyst efficiency η) and local variables (temperature T and n butane partial pressure $p_{C_4H_{10}}$).

It was found that the 1D models produced remarkably accurate results for both global and local variables. Either of the 1D model formulations gave rise to almost identical n butane partial pressure profiles, whereas profound differences in the prediction of temperature profiles were found. Due to the strong external heat transfer limitation the 1D models were sensitive to the energy balance boundary conditions. The two model formulations use different boundary conditions, with differences in the temperature profiles ensuing. Inhomogeneous values on the particle surface, such as temperature or concentration, added to the discrepancy between CFD and 1D results. Additionally, it was found that the 1D models were unable to describe inherently 3D phenomena such convective transport limitation due to channel blocking of the ring shaped catalyst.

We conclude that 1D models can accurately describe the catalyst particle behaviour for selective oxidation of n butane to MA under the variety of conditions found in an industrial MA reactor. However, exceptions have to be made for states where the boundary conditions are the determining factor, such as strong external transport limitation. In this case, the inability of 1D models to reflect the variety of surface values in one single boundary condition could potentially lead to errors, which boils down to the neglect of two spatial dimensions. Despite what has occasionally been claimed in the literature, the use of engineering correlations to determine transport parameters has not been found to contribute to model error in case of the flow around a single particle. These findings advocate for the investigation whether a 2D discretisation for the solid phase could improve the accuracy of continuum models for simulation of MA reactors. It has to be stressed that the findings presented in this work cannot be directly transferred to a full fixed bed reactor. For example, many particles in close proximity will influence the external flow around each other. Particles in direct contact with a cooled or heated reactor wall, enabling conductive heat transfer will exhibit even more pronounced heterogeneous temperature profiles than what was observed here. Therefore, further work on the comparison of experiments, CFD and continuum model simulations on the scale of entire fixed bed reactor is necessary to fully understand the capabilities and limitations of continuum models.

Nomenclature

Latin symbols

c	Concentration	$mol\,m^{-3}$
C_D	Drag Coefficient	
D	Diffusion Coefficient	$m^2\,s^{-1}$
E	Energy	J
H	Height	m
j	Diffusive Flux	$kg\,m^{-2}$
L	Length	m
M	Molar Weight	$kg\,mol^{-1}$
N	Molar Flux	$mol\,m^{-2}\,s^{-1}$
Nu	Nusselt number	
p	Pressure	Pa
q	Heat Flux	$W\,m^{-2}$
r	Radial Coordinate	m
$\widetilde{r}$	Dimensionless Radial Coordinate	
R	Radius	m
R_{gas}	Ideal Gas Constant	$J\,K^{-1}\,mol^{-1}$
r_g	Refinement Factor	
Re	Reynolds Number	
Sc	Schmidt Number	
u	Velocity	$m\,s^{-1}$
w	Mass Fraction	
S	Source Term	
T	Temperature	°C
V	Volume	m^3
x	Mole Fraction	
y^+	Dimensionless Wall Distance	

Greek symbols

α	Heat Transfer Coefficient	$W\,m^{-2}\,K^{-1}$
β	Mass Transfer Coefficient	$m\,s^{-1}$
γ	Factor	
δ	Kronecker Delta	
$\Delta_r H$	Heat of Reaction	$J\,mol^{-1}$
ϵ	Porosity	
η	Catalyst Effectiveness Factor	
ι	Boundary Layer Thickness	m
κ	Turbulent Kinetic Energy	$J\,kg^{-1}$
λ	Thermal Conductivity	$W\,m^{-1}$
μ	Dynamic Viscosity	Pa s
μ_t	Turbulent Eddy Viscosity	Pa s
ν	Stoichiometric Coefficient	
ξ	Tortuosity	
ρ	Density	$kg\,m^{-3}$
σ	Shape Factor	
τ	Stress Tensor	Pa
ϕ	Arbitrary Scalar	
Ω	Resistance	var.

Abbreviations

1D	One Dimensional
2D	Two Dimensional
3D	Three Dimensional
CFD	Computational Fluid Dynamics
MA	Maleic Anhydride
RANS	Reynolds averaged Navier Stokes
VPO	Vanadium Phosphorous Oxide

Subscripts

cat	Catalyst
E	Energy
eff	Effective
ext	External
diff	Diffusion
i	Species

int	Internal
j	Reaction
p	Particle
surf	Surface

CRediT authorship contribution statement

Scott D. Anderson: Conceptualization, Data curation, Formal analysis, Investigation, Methodology, Project administration, Software, Validation, Visualisation, Writing – original draft, Writing – review & editing. **Martin Kutscherauer:** Conceptualization, Data curation, Methodology, Software, Writing – review & editing. **Sebastian Böcklein:** Resources, Writing – review & editing. **Gerhard Mestl:** Resources, Writing – review & editing. **Thomas Turek:** Conceptualization, Supervision, Writing – review & editing. **Gregor D. Wehinger:** Conceptualization, Supervision, Writing – review & editing.

Declaration of competing interest

The authors declare that they have no known competing financial interests or personal relationships that could have appeared to influence the work reported in this paper.

References

Afandizadeh, S., Foumeny, E., 2001. Design of packed bed reactors: Guides to catalyst shape, size, and loading selection. Appl. Therm. Eng. 21 (6), 669–682. http://dx.doi.org/10.1016/S1359-4311(00)00072-7.

Aris, R., 1975. The Mathematical Theory of Diffusion and Reaction in Permeable Catalysts: The Theory of the Steady State, Vol. 1. Clarendon Press.

Bosanquet, C., 1944. The Optimum Pressure for a Diffusion Separation Plant, Vol. 27. British TA Report BR-507, Sep.

Brandstädter, W.M., Kraushaar-Czarnetzki, B., 2007. Maleic anhydride from mixtures of n-butenes and n-butane: simulation of a production-scale nonisothermal fixed-bed reactor. Ind. Eng. Chem. Res. 46 (5), 1475–1484. http://dx.doi.org/10.1021/ie061142q.

Burghardt, A., Kubaczka, A., 1996. Generalization of the effectiveness factor for any shape of a catalyst pellet. Chem. Eng. Process. Process. Intensif. 35 (1), 65–74. http://dx.doi.org/10.1016/0255-2701(95)04115-X.

Carberry, J., 1966. Yield in chemical reactor engineering. Ind. Eng. Chem. 58 (10), 40–53. http://dx.doi.org/10.1021/ie50682a009.

Clift, R., Grace, J.R., Weber, M.E., 2005. Spheres at higher Reynolds numbers. In: Bubbles, Drops, and Particles. Courier Corporation, pp. 97–141.

Dhole, S., Chhabra, R., Eswaran, V., 2006. A numerical study on the forced convection heat transfer from an isothermal and isoflux sphere in the steady symmetric flow regime. Int. J. Heat Mass Transfer 49 (5), 984–994. http://dx.doi.org/10.1016/j.ijheatmasstransfer.2005.09.010.

Diedenhoven, J., Reitzmann, A., Mestl, G., Turek, T., 2012. A model for the phosphorus dynamics of VPO catalysts during the selective oxidation of n-butane to maleic anhydride in a tubular reactor. Chem. Ing. Tech. 84 (4), 517–523. http://dx.doi.org/10.1002/cite.201100248.

Dixon, A.G., 2014. CFD study of effect of inclination angle on transport and reaction in hollow cylinder catalysts. Chem. Eng. Res. Des. 92 (7), 1279–1295. http://dx.doi.org/10.1016/j.cherd.2013.11.018.

Dixon, A.G., Ertan Taskin, M., Nijemeisland, M., Stitt, E.H., 2011. Systematic mesh development for 3D CFD simulation of fixed beds: Single sphere study. Comput. Chem. Eng. 35 (7), 1171–1185. http://dx.doi.org/10.1016/j.compchemeng.2010.12.006.

Donaubauer, P.J., Hinrichsen, O., 2019. Evaluation of effectiveness factors for multi-component diffusion models inside 3D catalyst shapes. Ind. Eng. Chem. Res. 58 (1), 110–119. http://dx.doi.org/10.1021/acs.iecr.8b04922.

Dong, Y., Geske, M., Korup, O., Ellenfeld, N., Rosowski, F., Dobner, C., Horn, R., 2018. What happens in a catalytic fixed-bed reactor for n-butane oxidation to maleic anhydride? Insights from spatial profile measurements and particle resolved CFD simulations. Chem. Eng. J. 350, 799–811. http://dx.doi.org/10.1016/j.cej.2018.05.192.

Dong, Y., Keil, F.J., Korup, O., Rosowski, F., Horn, R., 2016. Effect of the catalyst pore structure on fixed-bed reactor performance of partial oxidation of n-butane: A simulation study. Chem. Eng. Sci. 142, 299–309. http://dx.doi.org/10.1016/j.ces.2015.12.004.

Fairbanks, D.F., Wilke, C.R., 1950. Diffusion coefficients in multicomponent gas mixtures. Ind. Eng. Chem. 42 (3), 471–475. http://dx.doi.org/10.1021/ie50483a022.

Froment, G.F., Bischoff, K.B., De Wilde, J., 1990. Kinetics of heterogeneous catalytic reactions. In: Chemical Reactor Analysis and Design. Wiley New York, pp. 76–140.

Fuller, E.N., Ensley, K., Giddings, J.C., 1969. Diffusion of halogenated hydrocarbons in helium. The effect of structure on collision cross sections. J. Phys. Chem. 73 (11), 3679–3685. http://dx.doi.org/10.1021/j100845a020.

Fuller, E.N., Schettler, P.D., Giddings, J.C., 1966. New method for prediction of binary gas-phase diffusion coefficients. Ind. Eng. Chem. 58 (5), 18–27. http://dx.doi.org/10.1021/ie50677a007.

Gao, Z., Odstrcil, M., Böcklein, S., Palagin, D., Holler, M., Ferreira Sanchez, D., Krumeich, F., Menzel, A., Stampanoni, M., Mestl, G., et al., 2021. Sparse ab initio x-ray transmission spectrotomography for nanoscopic compositional analysis of functional materials. Sci. Adv. 7 (24), eabf6971. http://dx.doi.org/10.1126/sciadv.abf6971.

Gnielinski, V., 1975. Berechnung mittlerer Wärme- und Stoffübergangskoeffizienten an laminar und turbulent überströmten Einzelkörpern mit Hilfe einer einheitlichen Gleichung. Forschung Ingen. 41, 145–153.

Gnielinski, V., 1978. Gleichungen zur Berechnung des Wärme-und Stoffaustausches in durchströmten ruhenden Kugelschüttungen bei mittleren und großen Pecletzahlen. Verfahrenstechnik 12, 363–366.

Gnielinski, V., 1982. Berechnung des Wärme-und Stoffaustauschs in durchströmten ruhenden Schüttungen. Verfahrenstechnik 16, 36–39.

Hermans, I., Spier, E.S., Neuenschwander, U., Turrà, N., Baiker, A., 2009. Selective oxidation catalysis: Opportunities and challenges. Top. Catal. 52, 1162–1174. http://dx.doi.org/10.1007/s11244-009-9268-3.

Karthik, G., Buwa, V.V., 2019. Effect of particle shape on catalyst deactivation using particle-resolved CFD simulations. Chem. Eng. J. 377, 120164. http://dx.doi.org/10.1016/j.cej.2018.10.101.

Kutscherauer, M., Anderson, S.D., Böcklein, S., Mestl, G., Turek, T., Wehinger, G.D., 2023. A conjugated heat and mass transfer model to implement reaction in particle-resolved CFD simulations of catalytic fixed bed reactors. Preprint at https://chemrxiv.org/engage/chemrxiv/article-details/64c58e1ace23211b20c8414a.

Lecheler, S., 2014. Numerische Strömungsberechnung: Schneller Einstieg durch anschauliche Beispiele mit ANSYS 15.0. Springer-Verlag, Wiesbaden.

Lesser, D., 2016. Dynamic Behavior of Industrial Fixed Bed Reactors for the Manufacture of Maleic Anhydride (Dissertation). Technische Universität Clausthal.

Lesser, D., Mestl, G., Turek, T., 2017. Modeling the dynamic behavior of industrial fixed bed reactors for the manufacture of maleic anhydride. Chem. Eng. Sci. 172, 559–570. http://dx.doi.org/10.1016/j.ces.2017.06.049.

Maffei, T., Gentile, G., Rebughini, S., Bracconi, M., Manelli, F., Lipp, S., Cuoci, A., Maestri, M., 2016. A multiregion operator-splitting CFD approach for coupling microkinetic modeling with internal porous transport in heterogeneous catalytic reactors. Chem. Eng. J. 283, 1392–1404. http://dx.doi.org/10.1016/j.cej.2015.08.080.

Mariani, N., Keegan, S., Martinez, O., Barreto, G., 2003. A one-dimensional equivalent model to evaluate overall reaction rates in catalytic pellets. Chem. Eng. Res. Des. 81 (8), 1033–1042. http://dx.doi.org/10.1205/026387603322482266.

Mariani, N.J., Taulamet, M.J., Keegan, S.D., Martínez, O.M., Barreto, G.F., 2013. Prediction of effectiveness factor using one-dimensional approximations for complex pellet shapes and abnormal kinetics expressions. Ind. Eng. Chem. Res. 52 (44), 15321–15329. http://dx.doi.org/10.1021/ie4005805.

Marx, R., 2012. Kinetics of the Selective Oxidation of O-Xylene to Phthalic Anhydride (Dissertation). Technische Universität Clausthal.

Maußner, J., Freund, H., 2018. Efficient calculation of constraint back-offs for optimization under uncertainty: A case study on maleic anhydride synthesis. Chem. Eng. Sci. 192, 306–317. http://dx.doi.org/10.1016/j.ces.2018.06.079.

Mestl, G., Lesser, D., Turek, T., 2016. Optimum performance of vanadyl pyrophosphate catalysts. Top. Catalysis 59, 1533–1544. http://dx.doi.org/10.1007/s11244-016-0673-0.

M.Moghaddam, E., Foumeny, E., Stankiewicz, A., Padding, J., 2021. Heat transfer from wall to dense packing structures of spheres, cylinders and Raschig rings. Chem. Eng. J. 407, 127994. http://dx.doi.org/10.1016/j.cej.2020.127994.

Mocciaro, C., Mariani, N.J., Martínez, O.M., Barreto, G.F., 2011. A three-parameter one-dimensional model to predict the effectiveness factor for an arbitrary pellet shape. Ind. Eng. Chem. Res. 50 (5), 2746–2754. http://dx.doi.org/10.1021/ie101296d.

Müller, M., Kutscherauer, M., Böcklein, S., Mestl, G., Turek, T., 2020. On the importance of by-products in the kinetics of n-butane oxidation to maleic anhydride. Chem. Eng. J. 401, 126016. http://dx.doi.org/10.1016/j.cej.2020.126016.

Müller, M., Kutscherauer, M., Böcklein, S., Mestl, G., Turek, T., 2021. Improved kinetics of n-butane oxidation to maleic anhydride: The role of byproducts. Ind. Eng. Chem. Res. 60 (1), 218–229. http://dx.doi.org/10.1021/acs.iecr.0c05029.

Müller, M., Kutscherauer, M., Böcklein, S., Wehinger, G., Turek, T., Mestl, G., 2022. Modeling the selective oxidation of n-butane to maleic anhydride: From active site to industrial reactor. Catal. Today 387, 82–106. http://dx.doi.org/10.1016/j.cattod.2021.04.009.

National Research Council, 2001. Carbon Management: Implications for R&D in the Chemical Sciences and Technology. National Academies Press.

Petric, I., Karić, E., 2019. Simulation of commercial fixed-bed reactor for maleic anhydride synthesis: Application of different kinetic models and industrial process data. React. Kinetics Mech. Catal. 126, 1027–1054. http://dx.doi.org/10.1007/s11144-019-01533-9.

Ranz, W.E., Marshall, W., 1952. Vaporation from drops, part i. Chem. Eng. Prog. 48 (3), 141–146.

Reitzmann, A., Brandstädter, W.M., Streifinger, L., Estenfelder, M., 2016. Shaped catalyst body for flow-through fixed-bed reactors. In: Google Patents. US Patent 9, 409, 160.

Roache, P.J., 1998. Verification of codes and calculations. AIAA J. 36 (5), 696–702. http://dx.doi.org/10.2514/2.457.

Sharma, R.K., Cresswell, D.L., Newson, E.J., 1991. Kinetics and fixed-bed reactor modeling of butane oxidation to maleic anhydride. AIChE J. 37 (1), 39–47. http://dx.doi.org/10.1002/aic.690370103.

Siemens Digital Industries Software, 2020. Simcenter STAR-CCM+ Documentation. Siemens.

Siemens PLM, 2022. Simcenter STAR-CCM+ 2022.1. URL https://www.plm.automation.siemens.com/global/de/products/simcenter/STAR-CCM.html.

Sosna, B., Korup, O., Horn, R., 2020. Probing local diffusion and reaction in a porous catalyst pellet. J. Catalysis 381, 285–294. http://dx.doi.org/10.1016/j.jcat.2019.11.005.

Taulamet, M.J., Mariani, N.J., Martinez, O.M., Barreto, G.F., 2018. Prediction of effective reaction rates in catalytic systems of multiple reactions using one-dimensional models. Chem. Eng. J. 335, 876–886. http://dx.doi.org/10.1016/j.cej.2017.10.186.

Wehinger, G.D., Ambrosetti, M., Cheula, R., Ding, Z.-B., Isoz, M., Kreitz, B., Kuhlmann, K., Kutscherauer, M., Niyogi, K., Poissonnier, J., et al., 2022. Quo vadis multiscale modeling in reaction engineering?–A perspective review. Chem. Eng. Res. Des. http://dx.doi.org/10.1016/j.cherd.2022.05.0300.

Wellauer, T.P., Cresswell, D., Newson, E., 1986. Optimal policies in maleic anhydride production through detailed reactor modelling. Chem. Eng. Sci. 41 (4), 765–772. http://dx.doi.org/10.1016/0009-2509(86)87156-1.

Whitaker, S., 1972. Forced convection heat transfer correlations for flow in pipes, past flat plates, single cylinders, single spheres, and for flow in packed beds and tube bundles. AIChE J. 18 (2), 361–371. http://dx.doi.org/10.1002/aic.690180219.

Wijngaarden, R., Westerterp, K., 1993. A heterogeneous model for heat transfer in packed beds. Chem. Eng. Sci. 48 (7), 1273–1280. http://dx.doi.org/10.1016/0009-2509(93)81008-J.